Impact of Interactive Radiative Transfer on the Macroscopic Behavior of Cumulus Ensembles. Part I: Radiation Parameterization and Sensitivity Tests

KUAN-MAN XU AND DAVID A. RANDALL

Department of Atmospheric Science, Colorado State University, Fort Collins, Colorado

(Manuscript received 26 October 1993, in final form 5 July 1994)

ABSTRACT

Implementation of a broadband radiation parameterization in the UCLA cumulus ensemble model (CEM) is discussed in this study, with emphasis on the specific problems associated with adequate calculation of radiative transfer processes in the CEM. The radiation parameterization is based on the Harshvardhan et al. broadband radiative transfer model with cloud optical properties as formulated by Stephens et al. The lowest CEM layer is divided into a thick layer and a very thin layer near the surface for the longwave radiation calculation. Diagnostic tests have been performed to compare the accuracy of this parameterization with results from a more complicated radiative transfer model.

Simulations with fully interactive radiation are performed to compare two methods for invoking the radiation module. The time interval for calling the radiation module has to be very small for the conventional method, which keeps the radiative heating rate constant until the radiation module is called again. It can be larger for the "accumulated" method, which accumulates and averages cloud microphysical properties within the time interval and applies the amount of radiative heating over the time interval at the time when the radiation module is called. Additional sensitivity tests are also performed to justify the omission of the radiative effects of rapidly falling precipitating particles.

Other sensitivity tests are related to the adequacy of the domain size and horizontal resolution for studying the cloud–radiation interaction problems discussed in Part II.

1. Introduction

The role of clouds has gradually been recognized as a key uncertainty in studies of global climate system and climate sensitivity (e.g., Arakawa 1975; Cess et al. 1990). The interactions of clouds with solar and terrestrial radiation strongly influence the sensitivity of the global climate to external perturbations. Among the most important clouds for climate are the upper-tropospheric clouds associated with deep cumulus convection. Moist air detrained from deep cumulus towers forms horizontally extensive "anvil" clouds. These anvil clouds produce the stratiform precipitation associated with mesoscale convective systems (e.g., Houze 1977; Zipser 1977). They have a great influence on the evolution of the mesoscale convective system and the large-scale circulation in which they are embedded. The significance of the radiative effects of anvil clouds for the general circulation stems from their large areal coverage and long duration (Webster and Stephens 1980).

Recently, Xu et al. (1992) used the two-dimensional UCLA cumulus ensemble model (CEM), which covers a large horizontal area (~500 km) with a horizontal grid size small enough to resolve individual clouds, to study the macroscopic behavior of cumulus convection under a variety of large-scale and underlying surface conditions. They found that cumulus convection is rather strongly modulated by large-scale advective processes. The modulation exhibits some phase delays, however, when the basic wind shear is strong. This is presumably due to the existence of mesoscale convective organization.

The current study is designed to further explore the macroscopic behavior of cumulus ensembles by investigating the influence of cloud–radiation interactions on the collective effects of cumulus clouds. To do this, the UCLA CEM has been modified to include an interactive radiative transfer parameterization.

The details of the CEM have been described by Krueger (1988) and Xu and Krueger (1991). Briefly, the CEM is based on the anelastic system of dynamical equations with the Coriolis acceleration. It includes a third-moment turbulence closure (Krueger 1988) and a three-phase bulk cloud microphysics parameterization (Lin et al. 1983; Lord et al. 1984; Krueger et al. 1995). The sophisticated turbulence parameterization consists of 35 prognostic equations for second moments and third moments, and a diagnostic one for the turbulent length scale. The interactive radiation parameterization is based on Harshvardhan et al.'s (1987)

Corresponding author address: Dr. Kuan-Man Xu, Dept. of Atmospheric Science, Colorado State University, Fort Collins, CO 80523.

© 1995 American Meteorological Society

broadband radiative transfer model with cloud optical properties as formulated by Stephens et al. (1990). Part I of this two-part paper describes the radiation parameterization and sensitivity tests related to the implementation of the parameterization in the CEM. Part II (Xu and Randall 1995) will examine some hypothetical mechanisms for cloud–radiation interactions and the impact of interactive radiative transfer on the macroscopic behavior of cumulus convection.

The importance of cloud–radiation interactions for the macroscopic behavior of cumulus convection has previously been studied with observations (e.g., Gray and Jacobson 1977; Webster and Stephens 1980), numerical cloud models (e.g., Chen and Cotton 1988; Tao et al. 1991, 1993; Wong et al. 1993), and mesoscale models (e.g., Dudhia 1989; Churchill and Houze 1991; Miller and Frank 1993). One of the significant findings from the modeling studies is that the surface precipitation and the circulation in stratiform regions can be enhanced by longwave radiative transfer. For example, Tao et al. (1993) found that longwave radiation increased the surface precipitation rate by 14% in a simulated midlatitude squall system, and by 31% in a simulated tropical squall system. The increase occurs in both convective and stratiform regions of the squall systems. The inclusion of longwave radiative transfer can destabilize the atmospheric column. The increase of surface precipitation rate must, however, not be attributed to the cloud–radiation interactions alone, because noninteractive radiative cooling can also enhance the convective activity by destabilizing the large-scale environment (Dudhia 1989; Miller and Frank 1993; Xu and Randall 1995).

Hypothetical mechanisms for cloud–radiation interactions are related to the large horizontal/vertical inhomogeneity of the radiative heating rates due to the presence of clouds. They include the following: (i) horizontal differential heating between cloudy and clear regions (Gray and Jacobson 1977); (ii) continuously destabilizing effects of anvil cloud layers (Webster and Stephens 1980); and (iii) in-cloud radiative heating and radiative destabilization, generating buoyant turbulence in the anvil clouds (Lilly 1988). These are the topics studied in Part II.

The main purposes of Part I are (i) to present a radiation parameterization and sensitivity tests related to its implementation in the CEM, and (ii) to present some sensitivity tests related to the design of numerical simulations presented in Part II so that the discussion of cloud–radiation interaction mechanisms will be more clear.

Section 2 gives a brief description of the radiative transfer model. Section 3 outlines the implementation of the radiation parameterization in the CEM and comparison of the diagnostic tests obtained with this model with those of a complicated model. Results from the sensitivity tests are presented in section 4. Summary is given in section 5.

2. A simple broadband radiation parameterization

A broadband interactive radiative transfer model has been incorporated into the UCLA cumulus ensemble model (CEM), based on the work of Harshvardhan et al. (1987) with cloud optical properties as formulated by Stephens et al. (1990). This section gives a brief description of the radiative transfer model as currently implemented in the CEM.

Harshvardhan et al. (1987) developed a highly simplified broadband model to parameterize the transfer of solar and infrared radiation. This model was originally designed for use in general circulation models (GCMs). It accommodates variable cloud fractions and cloud properties and also is amenable to vectorization. This parameterization has been adopted because of its computational efficiency. No three-dimensional radiative transfer effects are included; the radiative transfer equation is solved one vertical column at a time.

a. Solar radiation

The solar (shortwave) radiation parameterization is an extension of that developed by Lacis and Hansen (1974). It takes into account Rayleigh scattering and absorption by water vapor (H_2O), carbon dioxide (CO_2), ozone (O_3), and clouds, as well as the solar zenith angle dependency of multiple scattering by clouds. No other gases or aerosols are considered. The δ–Eddington approximation (Joseph et al. 1976) and adding–doubling method (Lacis and Hansen 1974) are used to calculate the scattering from the direct beam and multiple scattering between layers. The values of the diffuse and direct albedos for wavelengths in the visible (<0.7 μm) and near-infrared (>0.7 μm) regions are treated as input variables and are functions of the solar zenith angle.

One major modification to the shortwave portion of the GCM radiation module (Harshvardhan et al. 1987, 1989) is in the treatment of cloud optical depth (τ_c), single scattering albedo (ω_0), and asymmetry factor (g). For example, in the GCM τ_c is parameterized using large-scale variables (Harshvardhan et al. 1989). In the CEM, these variables are directly related to cloud microphysical properties, as described in section 2c. Another modification is that additional layers have been added above the CEM top to more accurately determine the radiative heating rate (Q_R) in the layers near the model top (see section 3).

b. Infrared radiation

The infrared (longwave) radiation parameterization adopts the broadband transmission approach of Chou (1984) for H_2O, that of Chou and Peng (1983) for CO_2, and the method of Rodgers (1968) for O_3, as well as the water vapor continuum (e-type) absorption formula given by Roberts et al. (1976). The parameter-

ization includes the effects of both gaseous and hydrometeor absorption.

Gaseous absorption by H_2O, CO_2, and O_3 is taken into account. The treatment of H_2O and CO_2 is based on fitting functional forms to the band-averaged flux transmittance obtained by a line-by-line spectral integration for certain reference conditions. The spectral regions considered are centered 0–340 cm^{-1} and 1380–1900 cm^{-1} for H_2O bands, 620–720 cm^{-1} for CO_2 bands, and 980–1100 cm^{-1} for O_3 band. The water vapor continuum absorption over a wide spectral region (833–1250 cm^{-1}) is included, using the empirical formula for the absorption coefficient proposed by Roberts et al. (1976). The water vapor continuum absorption coefficient is highly temperature dependent and is also a function of wavelength in the spectral region.

Hydrometeor absorption is associated with water and ice clouds, as well as mixed phase (coexisting water and ice) clouds. The absorption due to precipitating particles (rain, snow, and graupel) is neglected in the CEM, except for that due to snow. The justification for this approximation will be provided in sections 3 and 4. The existence of clouds complicates the computational procedure for the upward/downward flux. Harshvardhan et al. (1987) used a computational scheme utilizing the probability of a clear line of sight between each layer and all other layers, the ground, and the top of the atmosphere. Then, the cloudy sky fluxes are computed from the same set of equations as the clear sky fluxes, with certain multiplicative cloudiness factors. The cloudiness factors depend on the probabilities of clear line of sight between levels, that is, the cloud fraction in each layer and the degree of cloud vertical overlap. Both maximum and random vertical overlaps are allowed.

Several modifications to the longwave portion of the GCM radiation module have been made: (i) the cloud emissivity (ϵ) has been reformulated, based on Stephens et al. (1990); (ii) the calculation of planetary boundary layer (PBL) stratus heating and cooling has been deleted; and (iii) the lowest model layer is now divided into two sublayers to more accurately determine the radiative heating rate (see section 3).

c. *Cloud optical properties*

Stephens et al. (1990) used the anomalous diffraction theory of van de Hulst (1957) to determine the scattering extinction efficiencies as a function of wavelength, refractive index, and the cross-sectional area of the particle size distribution. A modified Gamma function,

$$n(r) = \frac{N_0}{\Gamma(p) r_w} \left(\frac{r}{r_w}\right)^{p-1} \exp\left(-\frac{r}{r_w}\right), \quad (1)$$

is used to characterize the size distribution of cloud droplets with radius of r, where N_0 is the total volume concentration of particles, r_w is a characteristic radius of the distribution, p is the dispersion of the distribution, and $\Gamma(p)$ is the Gamma function. For precipitating particles, the Marshall–Palmer (1948) distribution is used; that is, $p = 1$. For nonprecipitating particles, p is chosen to be 7, following Wong et al. (1993).

For a given cloud water content q_w, where the subscript w can be replaced by c for cloud water, i for cloud ice, or s for snow, the cross-sectional area per unit volume of the distribution is

$$A = \frac{3}{4} \frac{q_w}{\rho_w} \frac{f(2)}{r_w f(3)}, \quad (2)$$

where ρ_w is the density of the particle, and $f(2)$ and $f(3)$ are related to the gamma function.

The volume extinction efficiency α_{ext} can be expressed as (Stephens et al. 1990)

$$\alpha_{ext} = 2A + \frac{4A}{f(2)} \mathrm{Re}\left[\frac{p}{u_w(u_w + 1)^{p+1}} + \frac{1}{u_w^2(u_w + 1)^p} - \frac{1}{u_w^2}\right], \quad (3)$$

where Re[ ] denotes the real part of the factor in square brackets, $u_w = 2x_w(n - 1)$, $x_w = 2\pi r_w/\lambda$, n is the complex index of refraction ($n' - in''$), and λ is a typical wavelength of solar radiation. Because the Harshvardhan et al. (1987) radiative transfer model has one broad band, the wavelength dependency of α_{ext} is neglected. Thus, a constant wavelength ($\lambda = 1.38$ μm) and the corresponding n' and n'' for cloud water, cloud ice, and snow are chosen in the calculation of α_{ext}. We set n' to 1.32247 for cloud water, and 1.28852 for cloud ice/snow, while n'' is 0.8157×10^{-4} for cloud water, and 0.1580×10^{-4} for cloud ice/snow.

Then, the cloud optical depth (τ_c) is the integration of volume extinction efficiency; that is,

$$\tau_c = \int \alpha_{ext} \rho dz, \quad (4)$$

where ρ is the air density and dz is the layer thickness. Following Harshvardhan et al. (1989), the cloud (upward or downward) emissivity is expressed as

$$\epsilon = 1 - \exp(-0.75\tau_c). \quad (5)$$

For mixed phase clouds, the cloud optical depth is the sum of that of all water species. The cloud emissivity is calculated from (5) based on the total cloud optical depth. The single scattering albedo (ω_0) and asymmetry factor (g) are the weighted average of those of cloud water, cloud ice, and snow using α_{ext} and N_0 as their respective weighting functions; that is,

$$\omega_0 = (\alpha_{ext_c}\omega_{0_c} + \alpha_{ext_i}\omega_{0_i} + \alpha_{ext_s}\omega_{0_s})/(\alpha_{ext_c} + \alpha_{ext_i} + \alpha_{ext_s}), \quad (6)$$

$$\tau_c = \tau_{c_c} + \tau_{c_i} + \tau_{c_s}, \quad (7)$$

$$g = (g_c N_{0_c} + g_i N_{0_i} + g_s N_{0_s})/(N_{0_c} + N_{0_i} + N_{0_s}), \quad (8)$$

where $g_c = 0.85$, $g_i = 0.70$, $g_s = 0.70$, $\omega_{0_c} = 0.99$, $\omega_{0_i} = 0.97$, and $\omega_{0_s} = 0.97$; N_{0_c}, N_{0_i}, and N_{0_s} are the total volume concentration of cloud water, cloud ice, and snow, respectively. The volume concentration (N_{0_w}, where $w = c$, i, or s) is determined from

$$q_w = \frac{4}{3}\pi\rho_w N_{0_w} r_m^3 f(3). \quad (9)$$

The above formulation of cloud optical properties is tailored to this particular radiation parameterization. There are many different formulations used in a variety of radiation parameterizations (e.g., Duhdia 1989; Fu and Liou 1993; Held et al. 1993; Sui et al. 1994). The formulation is also limited by the bulk microphysics parameterization of the CEM, in particular, the inconsistent cloud/ice particle size distributions, monodisperse versus modified Gamma, assumed in the microphysics and radiation parameterizations, respectively.

3. Implementation of the radiation parameterization

a. An additional layer near the ground

The atmospheric boundary layer is characterized by a large temperature gradient in the lowest one meter (Fig. 1). The accuracy of the longwave radiation heating rate Q_{LW} for the lowest model layer, especially in the convectively disturbed regions, is questionable. That is, Q_{LW} is very sensitive to the choice of near-surface air temperature in the Harshvardhan et al. (1987) model. Therefore, the longwave radiation code has been modified by dividing the lowest model layer into a thick layer, which has a well-mixed structure in potential temperature and water vapor mixing ratio and a very thin (~1 m) layer near the surface, which is characterized by large gradients in potential temperature and water vapor mixing ratio (Fig. 1).

The height of the thin layer has been determined empirically and is a function of the Monin–Obukhov length (Fu et al. 1995). Fu et al. determined this height as that for which the temperature obtained from the similarity profile when used as the surface air temperature in the radiation code gives the same Q_R for the lowest CEM layer as that calculated using the similarity profile with 1-m resolution for the radiation code. The empirical function is

$$z_p = 0.2766 + 0.2324 \log(|L|), \quad (10)$$

where L is the Monin–Obukhov length. From the similarity profile, the potential temperature and water vapor mixing ratio at z_p (θ_{sa} and q_{sa}) can be obtained:

$$\theta_{sa} = \theta_g + (\theta_m - \theta_g) C_\theta(z_p, z^*, L)/C_\theta(z_m, z^*, L), \quad (11)$$

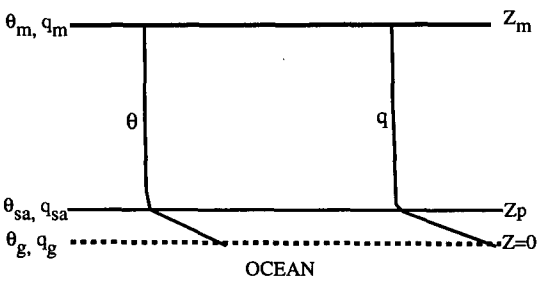

FIG. 1. A schematic diagram for illustrating the potential temperature and water vapor mixing ratio structures in the lowest model layer, which is divided into two sublayers for the longwave radiation computation. See text for an explanation of the notations.

$$q_{sa} = q_g + (q_m - q_g) C_\theta(z_p, z^*, L)/C_\theta(z_m, z^*, L). \quad (12)$$

Here subscripts g and m stand for ground and mean value at the lowest model layer, respectively, z^* is the roughness length, and C_θ is the coefficient of heat transfer as determined following Businger (1973).

The longwave heating rate in the lowest CEM layer is then the mass-weighted average of those in the two sublayers.

b. Additional layers above the model top

Because of the limited domain depth of the model, the accuracy of solar radiative heating rates Q_{SW} near the model top is not satisfactory. A standard approach is to add extra layers above the model top for the solar radiation computation (e.g., Wong et al. 1993).

Two extra layers (at 20 and 26 km) are now added to the Harshvardhan et al. (1987) model for simulation of deep convection. These extra layers have the same temperature as that at the top of the model but a smaller amount of water vapor (exponentially decreased) than that at the top of the model. At the model top Q_{SW} does not vary much as the top layer moves higher than 26 km. For consistency, these extra layers are also included in the longwave portion of the code; Q_{LW} is not affected at all.

For simulations of shallow stratocumulus clouds, observed temperature and water vapor profiles above the model top are used. There are usually many additional layers (~10) above the model top, depending on the location of the model top. In this type of simulation, the additional layers in the LW calculation do affect Q_{LW} in the layers near the model top because the model domain depth is very shallow (~5 km).

c. Comparison with a multiband model

The validity of the broadband radiation parameterization as presented in section 2 has been examined through comparison of its results with those of a multiband radiative transfer model. This multiband model

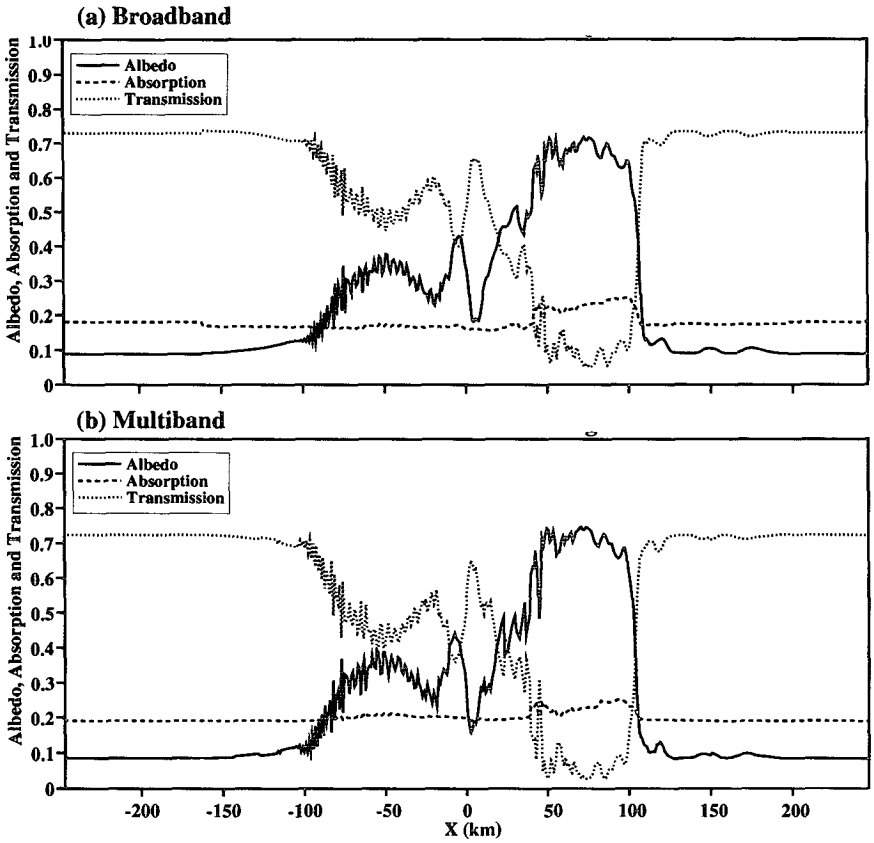

FIG. 2. Shortwave albedo at the top of the atmosphere, solar transmission to the surface, and shortwave absorption within the atmosphere, as diagnosed by (a) the broadband model and (b) the multiband model of Wong et al. The convective region is from 30 to 106 km, stratiform region from −80 to 29 km, and thin-anvil regions from −166 to −79 km and from 107 to 186 km. The remainder is the clear sky region.

was used by Wong et al. (1993) to diagnose the radiative budgets of a tropical mesoscale convective system. Briefly, it is based on the two-stream plane-parallel radiative transfer model developed by Stackhouse and Stephens (1991). The physical processes such as absorption and scattering by both molecules and particles are treated in a consistent way. The particulate optical properties are determined using Mie solutions assuming equivalent-diameter spheres from the particle size spectrum. The gaseous absorption is calculated using the k-distribution method for H_2O, CO_2, and O_3 in both the solar and infrared spectra, as well as O_2 absorption in the solar spectrum. Parameterizations of e-type absorption and Rayleigh scattering are also included.

The multiband model includes 14 bands in the solar spectrum and 10 bands in the infrared spectrum. The particulate optical properties are thus dependent on wavelength. This is one of the fundamental differences between the two radiative transfer models. In the broadband model, the particulate optical depths are calculated from a typical wavelength (see section 2c) and the single scattering albedos are prescribed to be constants for different water species. Another difference is that an observed size distribution for ice was used by Wong et al. (1993). This difference may also have some impact on the results.

The data used for comparison are from a simulation of tropical mesoscale convective systems during the Equatorial Mesoscale Experiment (EMEX) using a two-dimensional cloud model (Wong et al. 1993). A brief comparison is presented below. Figure 2 shows a comparison of shortwave albedo at the top of the atmosphere, solar transmission to the surface, and shortwave absorption within the atmosphere (all are "normalized") at 0816 local time. The radiative effects of all hydrometeors (cloud water, cloud ice, snow, graupel, and rainwater) are included in both radiative transfer models. The agreement of the results from the two models is very good except for the stratiform region near $x = -50$ km. The difference may be due to the different ice size distributions used in the models because cloud ice is the main hydrometeor around 8 km height in this region (Fig. 3a in Wong et al. 1993). A

Q_{SW} difference of 0.7 K d^{-1} between 7 and 12 km also occurs in the stratiform region, as shown later.

Figure 3 shows plots similar to those in Fig. 2a except for the differences due to neglecting the radiative effects of all precipitating particles (rainwater, graupel, and snow) or rapidly falling precipitating particles (rainwater and graupel). As expected, some differences occur mainly in the convective region when the radiative effects of all precipitating particles are neglected. The albedo and transmission differ by about 0.02, while the difference in absorption is less than 0.005. When the radiative effects of rapidly falling precipitating particles are neglected, the albedo and transmission differ by less than 0.002 and no difference in absorption is observed in any region. Therefore, the radiative effects of rainwater and graupel can be neglected, while those of snow are retained in the broadband parameterization. Further justification of this approximation will be presented in section 4c, based on a comparison of two pairs of simulations.

The vertical profiles of Q_{SW} and Q_{LW} for the clear sky, thin-anvil, stratiform, and convective regions of the simulated mesoscale convective system are generally in good agreement between the two radiative transfer models (Fig. 4), although some differences appear at selected levels (e.g., Q_{SW} at 6–12 km in the stratiform region, Q_{LW} in clear sky and thin-anvil regions). The sum of Q_{SW} and Q_{LW} does not show significant difference in the convective and stratiform regions despite some large differences in Q_{SW} and Q_{LW} at selected levels. This suggests that the broadband model can basically reproduce the net radiative effects as far as the diagnostic tests are concerned.

d. Methods for invoking the radiation parameterization

The conventional way to invoke a radiation parameterization (e.g., Dudhia 1989; Sui et al. 1994) is as follows. The radiation module is called once every few dynamical time steps and Q_R is kept *constant* over the following dynamical time steps until the radiation module is called again. Let the dynamical time step be Δt, and the time interval for invoking the radiation module be ΔT. Since cloud cells move rapidly in the domain, they will not stay in the same grid cell within ΔT if ΔT is greater than $\Delta x/U$, where Δx is the grid size of a cloud model and U is the propagation speed of cloud cells. A stricter requirement for eliminating the spatial errors of the time-averaged Q_R (over ΔT) would be

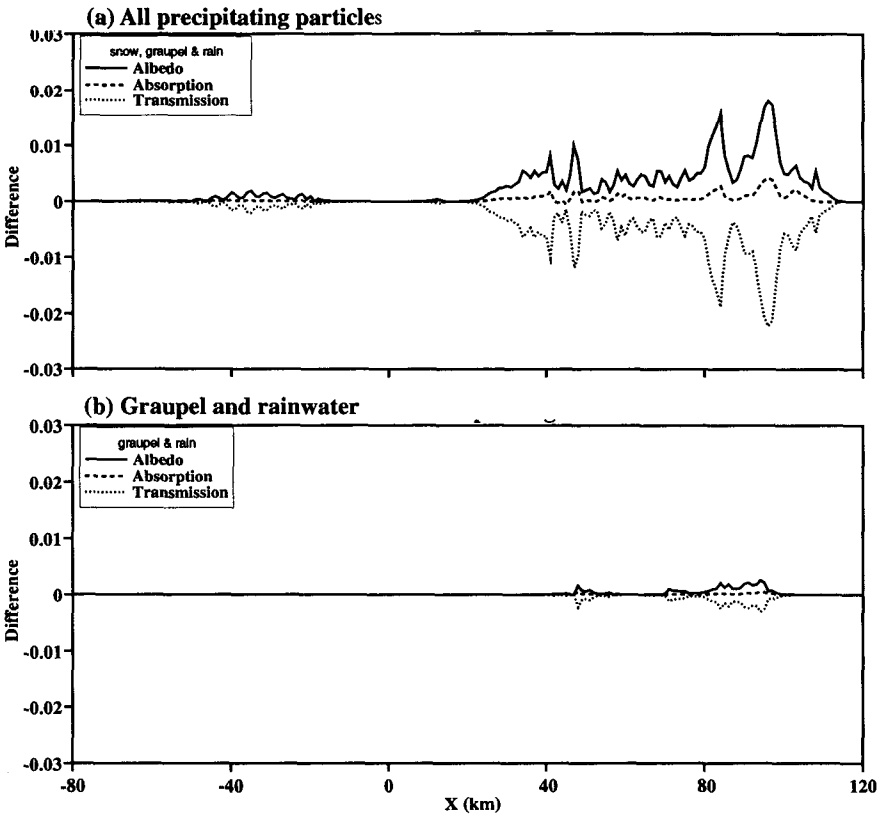

FIG. 3. Same as Fig. 2a except for the differences by neglecting (a) all precipitating particles and (b) graupel and rainwater only. A portion of the domain shown in Fig. 2 has significant differences.

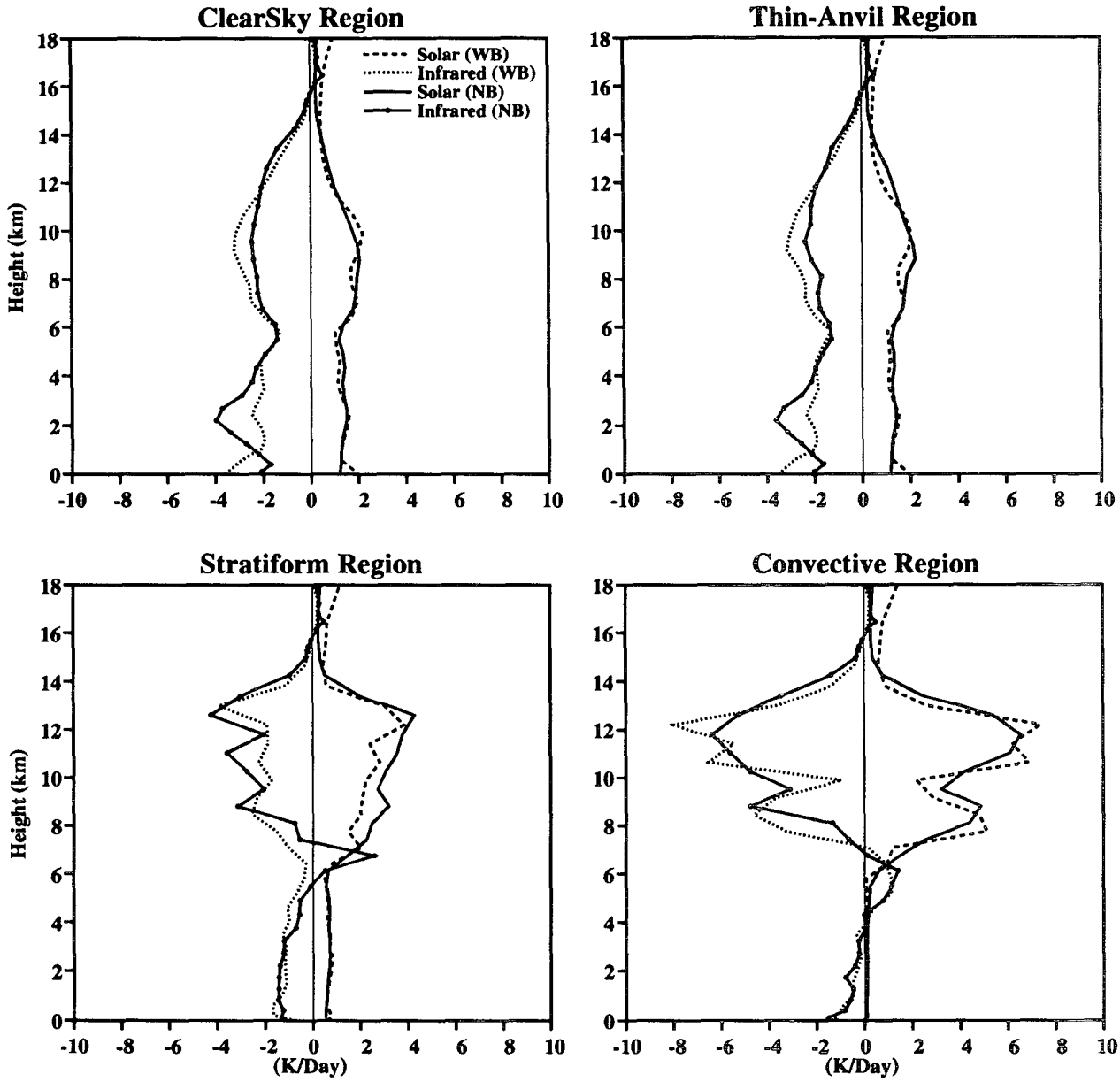

FIG. 4. Solar and infrared radiative heating rates for clear sky, thin-anvil, stratiform, and convective regions from the broadband (WB) and multiband (NB) radiative transfer models. See the caption of Fig. 2 for the corresponding areas of each region.

$$\Delta T \leq \frac{1}{2}\Delta x/U. \tag{13}$$

For example, let $\Delta x = 2000$ m and $U = 15$ m s^{-1}; ΔT should be less than 1 min. This is not sufficiently economical. When Δx is small and U is large, ΔT has to be very small. The issue of eliminating the spatial errors of the time-averaged Q_R (over ΔT) due to infrequent computation of radiative transfer processes in explicit simulations of cumulus convection has not been raised before. Table 1 shows some examples of ΔT used in previous modeling studies and the required ΔT based on (13). Note that the U used to construct the table is the propagation speed of cloud systems, not that of individual cloud cells. The latter is usually much larger. Thus, the required ΔT based on cloud-cell propagation speeds should ideally be much smaller than that shown in Table 1.

Alternate ways for invoking the radiation module, which would possibly allow the use of larger ΔT, are the "pulsed" and "accumulated" methods. The pulsed method is identical to the conventional method except that the amount of radiative heating over ΔT, that is, $Q_R\Delta T$, is applied at the time when the radiation module

TABLE 1. Comparison of studies regarding ΔT.

Study	ΔX (m)	U (m s^{-1})	Required ΔT (s)	Actual ΔT (s)
Tao et al. (1991)	750	14.5	26	120–180
Chen and Cotton (1988)	1500	6	125	not available
Sui et al. (1994)	1500	8	94	180
Held et al. (1993)	5000	6	417	6000

is called, and then Q_R is set to zero for the following dynamical time steps until the radiation module is called again. The accumulated method is identical to the pulsed method except that the accumulated and averaged cloud microphysical properties (cloud water, cloud ice, and snow mixing ratios) are used as input to the radiation module. The spatial errors of the time-averaged Q_R (over ΔT), as mentioned above, are basically eliminated because the same amount of cloud optical properties (over ΔT) is included when the radiation module is called every Δt. If ΔT is very long, however, temporal errors may be introduced because the amount of radiative heating is only applied every ΔT. Comparison of results using the conventional and accumulated methods will be presented in section 4b. The pulsed method will not be discussed because the spatial errors of the time-averaged Q_R are almost as large as those using the conventional method.

4. Sensitivity tests

a. Basic design

Tests of the radiation parameterization were performed with a time-independent x component of geostrophic wind (i.e., the large-scale pressure gradient) and time-varying large-scale advective effects. All of these variables are horizontally uniform in the CEM. The vertical profile of the geostrophic wind is typical of the 11 September 1974 squall line environments observed during the GATE [GARP (Global Atmospheric Research Program) Atlantic Tropical Experiment] Phase III (Fig. 1b in Xu et al. 1992). The vertical profiles of the large-scale advective effects are observed means for GATE Phase III (Fig. 1c in Xu et al. 1992). The large-scale advective effects are constant for the first 6 hours and afterward vary sinusoidally with a period of 32 h (dotted line in Fig. 5a). Thus, the modulation of convective activity by large-scale advective effects can be simulated and the difference between the control and each sensitivity test can be seen from that in the degree of modulation.

The remaining aspects of the sensitivity tests are identical to those described by Xu et al. (1992), unless mentioned otherwise. For example, the domain size is 512 km, with a horizontal grid size of 2 km. A stretched coordinate of 33 layers is used with thickness from 100 m at the model bottom to 1000 m at the model top (at ~19 km). The underlying surface is the ocean with a *fixed* sea surface temperature of 299.9 K.

All simulations were run for 24 h of physical time with a time step of 10 s. The initial thermodynamic conditions are horizontally uniform. Thus, some perturbations of temperature usually have to be introduced to initiate clouds in CEMs [see Xu (1993) for a review of other methods]. Because of the short period of the simulations presented in this study, small, random temperature perturbations into the lowest model layer as used in Xu et al. (1992) will take too long to initiate clouds. Thus, a "gust front type" temperature perturbation is introduced after the first 1000 s of integration for a period of 1000 s in all simulations. The magnitude of maximum heating/cooling rate is 0.0033 K s^{-1}. The temperature perturbation is restricted to a region of 45 km wide and 2 km deep. It decreases exponentially in both horizontal directions but is height independent. This method is not identical to the "cool pool" method (Tao et al. 1991) since the domain-averaged temperature is the same as in the initial sounding with the current method. The principle of discontinuous horizontal temperature distributions to initialize convective circulations is similar.

b. Conventional versus accumulated methods

Seven sensitivity tests were performed to compare the conventional and accumulated methods and to determine the optimum value of ΔT. The control uses 10 s as the time interval (ΔT) for invoking the radiation module, which is identical to the dynamics time step. This run is called C0. For each method, three additional tests were performed with ΔT of 1 min, 2 min, and 5 min, respectively. These tests are called C1, C2, and C5 for the conventional method and A1, A2, and A5 for the accumulated method. All other aspects of the design of simulations are identical between C0 and each sensitivity test (see Table 2).

Figure 5 shows the domain- and hourly averaged surface precipitation rate, $\langle P \rangle$, for C0 (solid curve on each

TABLE 2. Description of sensitivity tests.

Test	Domain (km)	ΔX (km)	ΔT (s)	Method	Cloud optical properties
C0	512	2	10	conventional	q_c, q_i, q_s
C1	512	2	60	conventional	q_c, q_i, q_s
C2	512	2	120	conventional	q_c, q_i, q_s
C5	512	2	300	conventional	q_c, q_i, q_s
A1	512	2	60	accumulated	q_c, q_i, q_s
A2	512	2	120	accumulated	q_c, q_i, q_s
A5	512	2	300	accumulated	q_c, q_i, q_s
C0GR	512	2	10	conventional	q_c, q_i, q_s, q_g, q_r
C1GR	512	2	60	conventional	q_c, q_i, q_s, q_g, q_r
A2DD	1024	2	120	accumulated	q_c, q_i, q_s
A1HX	512	1	60	accumulated	q_c, q_i, q_s

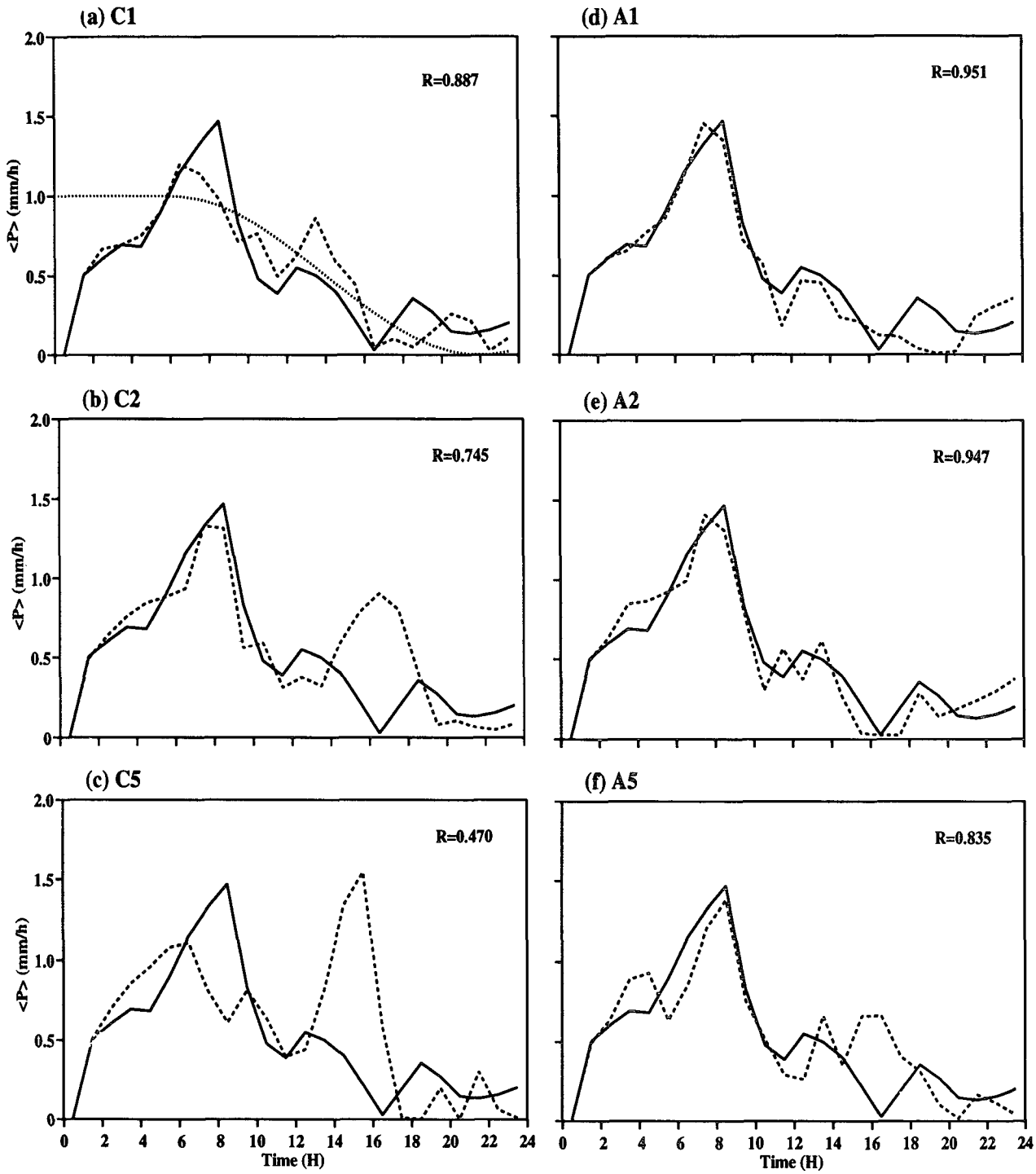

FIG. 5. Time sequence of the domain- and hourly averaged surface precipitation rate for six simulations (dashed line) as labeled on each plot. The solid curve is for C0 and the dotted line in (a) is the time variation of imposed large-scale advective effects; R is the correlation coefficient between C0 and each sensitivity test.

plot), C1, C2, C5, A1, A2, and A5. The correlation coefficient of $\langle P \rangle$ between C0 and each sensitivity test R is also shown on the plots. First, let us examine the degree of modulation in C0. The surface precipitation rate increases during the first 9 h and basically decreases afterward, as the large-scale advective effects

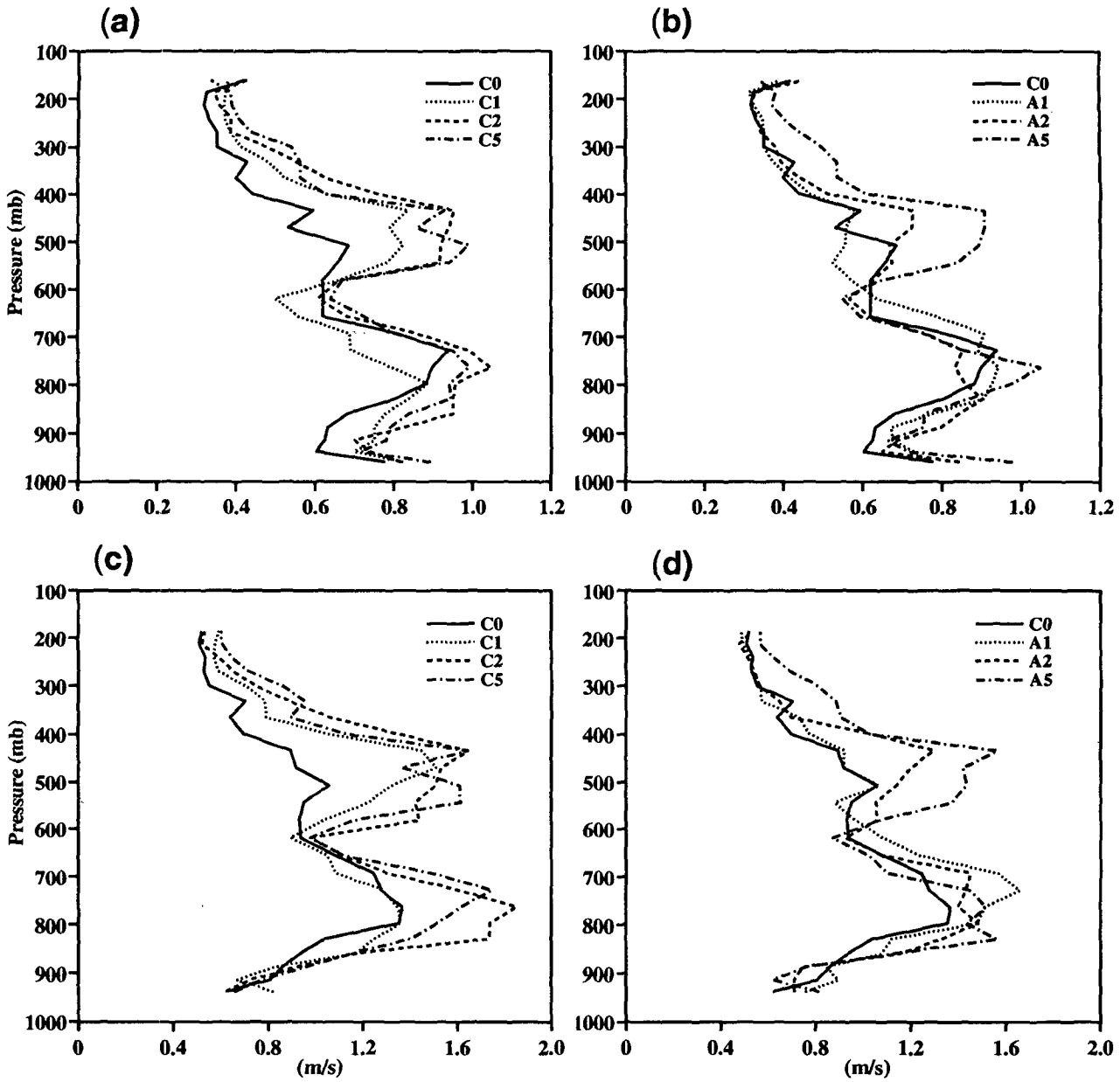

FIG. 6. Vertical profiles of median (50% level), mean vertical velocity of clouds for (a) C0, C1, C2, and C5, and (b) C0, A1, A2, and A5. Panels (c) and (d) are respectively identical to (a) and (b) except for the maximum vertical velocity of clouds, at least 4 km wide.

decrease (dotted line in Fig. 5a). Therefore, the degree of modulation is reasonably strong for C0.

Secondly, the comparison between C0 and each sensitivity test is described. In C1, the time variation of $\langle P \rangle$ is very similar to that in C0 except for a slightly weaker peak at 9 h and a slightly stronger one at 14 h. The time variation of $\langle P \rangle$ in C2 is basically similar to that in C0 before 14 h. The main difference between C2 and C0 is the peak at $\sim$17 h when the large-scale advective effects are weak. The difference between C5 and C0 is much greater. For the accumulated method, $\langle P \rangle$ of all three simulations (A1, A2, and A5) is very similar to that of C0. At 16 h when $\langle P \rangle$ of C0 is a minimum A5 shows a secondary peak. This difference is similar with that between C2 and C0 except with a smaller magnitude.

In summary, it is apparent that the value of ΔT affects the time variation of the intensity of convection as measured by $\langle P \rangle$; that is, (i) the result is more dissimilar to that of C0 as ΔT increases and (ii) for a given ΔT, $\langle P \rangle$ obtained from the accumulated method is much more similar to that of C0 than that from the

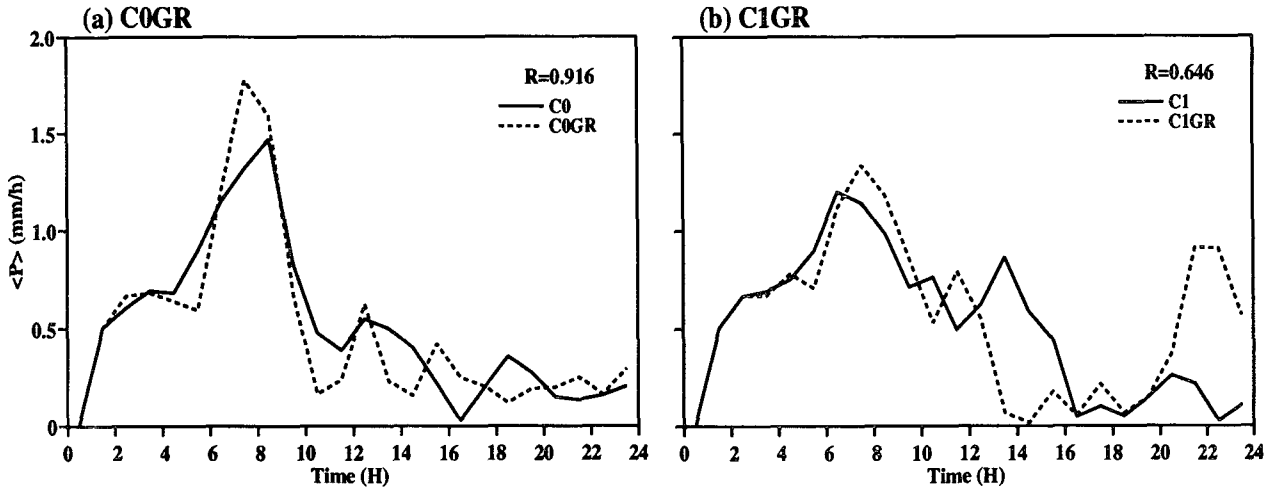

FIG. 7. Same as Fig. 5 except for (a) C0GR and (b) C1GR.

conventional method. Therefore, a larger ΔT can be used with the accumulated method than with the conventional method. In C0 the propagation speed of the cloud cells is ~ 11 m s^{-1}, and thus ΔT from (13) is 90 s. This may explain why the results from C1 are reasonably good but those from C2 are not. The optimum value of ΔT for the conventional method is thus determined by (13). That for the accumulated method can be twice as large (180 s).

The adequacy of either method has to be gauged by some statistics of the size and intensity of clouds. Figures 6a and 6b show the median (50% level), mean vertical velocity of clouds; that is, the mean vertical velocity of 50% of clouds is stronger/weaker than the median value. This statistic is similar to that presented by LeMone and Zipser (1980) with observed data except that strong drafts (>1 m s^{-1}) were examined. A CEM grid point is identified as "cloudy" if the sum of cloud water and cloud ice mixing ratios exceeds 1% of saturation water vapor mixing ratio and the vertical velocity is positive. An average is taken for adjacent cloudy grid points at a given level to obtain the mean vertical velocity of a cloud, as well as the size of the cloud. The reason for showing Fig. 6 is to compare the

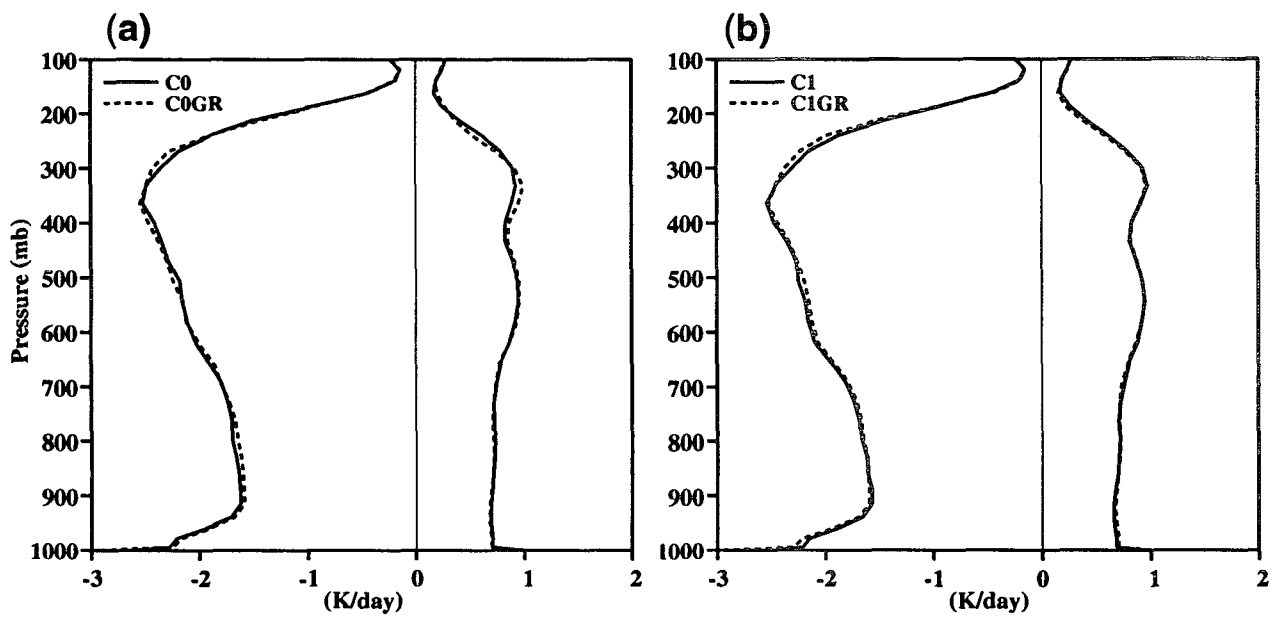

FIG. 8. Vertical profiles of shortwave and longwave heating rates averaged over the entire domain and entire integration period for (a) C0 and C0GR, and (b) C1 and C1GR.

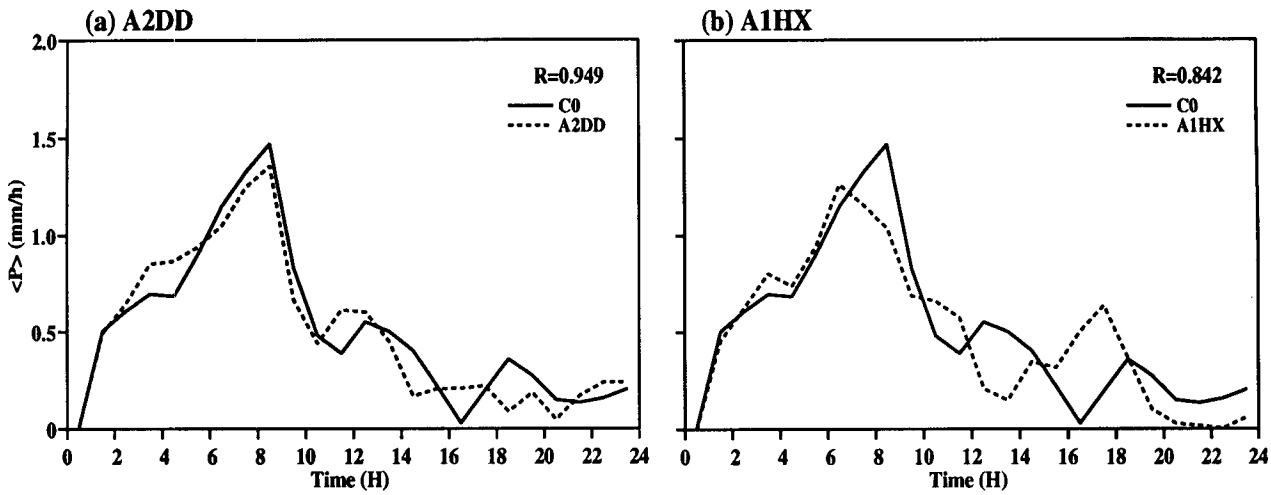

FIG. 9. Same as Fig. 5 except for (a) A2DD and (b) A1HX.

results among the sensitivity tests, not with observations.

Figures 6a and 6b indicate that the differences between C0 and each sensitivity test occur mainly above 600 mb, especially between 400 and 600 mb. The mean vertical velocity of clouds is generally stronger for larger ΔT, especially with the conventional method. Smaller differences are also apparent in the lower troposphere between C0 and each sensitivity test. Overall, the differences of A1 and A2 from C0 are the smallest among the tests. The statistic for the maximum vertical velocity within a cloud at least 4 km wide (i.e., at least two grid points) is similar to that of the mean vertical velocity (Figs. 6c and 6d). Therefore, the results in Fig. 6 basically reconfirm the conclusion obtained earlier from the examination of the modulation of convective activity.

A possible explanation for the results shown in Fig. 6 is as follows. The clear region on the upstream side of a moving cloud cell gains extra destabilization due to radiation. The buoyancy of the cloud is thus slightly larger except for near the cloud-base level. On the downstream side of the cloud cell, the cloud layer loses the radiative destabilizing effects, which will not affect the strength of the cloud instantaneously (Xu and Randall 1995). Thus, the strength of drafts becomes stronger as ΔT increases. This explanation may also be supported by the 24-h averaged $\langle P \rangle$ (0.508, 0.512, 0.553, 0.558 mm h^{-1} for C0, C1, C2, and C5, respectively), which is larger for larger ΔT.

A similar statistical analysis for the median cloud diameter is not possible due to the coarse horizontal resolution used in the simulations. Thus, the mean cloud diameter was calculated rather than the median diameter. No systematic differences between C0 and any sensitivity test were found (not shown).

c. *The radiative effects of rapidly falling precipitating particles*

The radiative effects of graupel and rainwater particles are included in C0GR and C1GR, which will be compared with C0 and C1, respectively (Table 2). In the diagnostic test described in section 3, the radiative effects of graupel and rainwater particles were found to be basically negligible. In prognostic tests, one has to be concerned with the large terminal velocities of these particles, which are on the order of 10 m s^{-1}. The typical vertical resolution (Δz) in the CEM is 500 m ($\sim$100 m in the lowest 1 km of the CEM); then it will take only 50 s for the graupel/rainwater particles to fall to a lower level. Therefore, the radiation module with the effects of rapidly falling precipitating particles has to be called more frequently, based on the argument related to (13). That is, ΔT should be less than 25 s, by replacing U with the terminal velocity and Δx by Δz in (13), respectively.

Figure 7 shows $\langle P \rangle$ for C0, C0GR, C1, and C1GR. The basic features of the time evolution of $\langle P \rangle$ are rather similar between C0 and C0GR. The similarity also exists for the first 12 h of C1 and C1GR. The differences between C1 and C1GR become larger afterward, however. This is also indicated by the correlation coefficient, which is smaller than that between C0 and C0GR (0.646 vs 0.916). In addition, the 24-h averaged $\langle P \rangle$ does not differ much between C0 and C0GR (0.508 vs 0.493 mm h^{-1}), but it is larger in C1GR than in C1 (0.550 vs 0.512 mm h^{-1}). These results suggest that a proper inclusion of the radiative effects of rapidly falling precipitating particles requires a very small ΔT. Otherwise, the impact of improper inclusion is far greater than that by totally neglecting those effects. A possible explanation is that if ΔT is larger the radiative effects may be exaggerated within

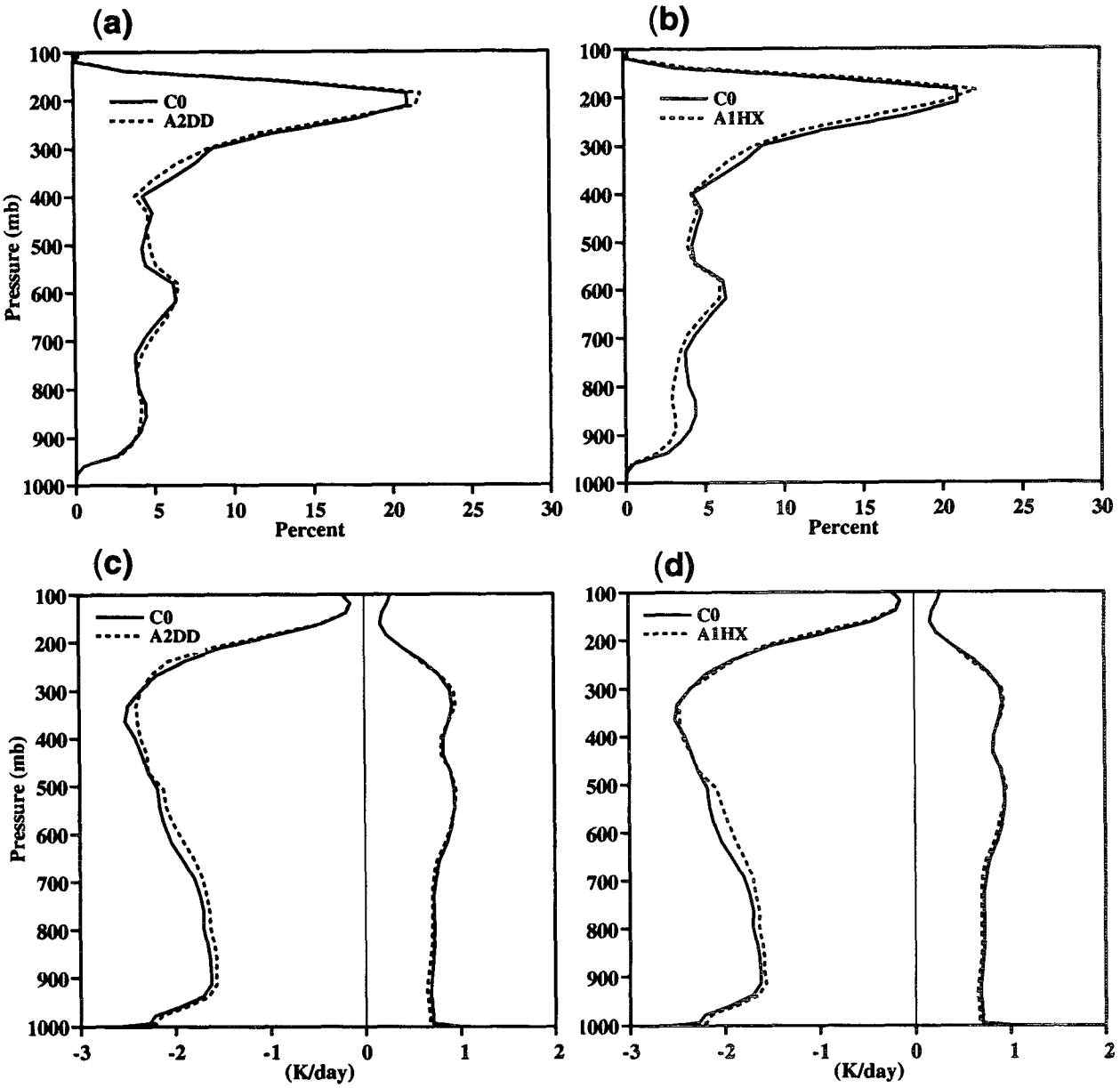

FIG. 10. Vertical profiles of fractional cloudiness for (a) C0 and A2DD, and (b) C0 and A1HX averaged over the entire domain and entire integration period. Panels (c) and (d) are respectively identical to (a) and (b) except for shortwave and longwave heating rates.

the layers where rapidly falling precipitating particles just form.

Figure 8 shows a comparison of Q_{SW} and Q_{LW} averaged over the entire domain and entire integration period between these two pairs of simulations. There are almost no systematic differences between each pair of simulations.

In summary, the radiative effects of rapidly falling precipitating particles have been demonstrated to be basically negligible. A proper inclusion of these effects would require invoking the radiation module much more frequently. Therefore, we do not include them.

d. Horizontal domain size and resolution

Two simulations have been performed to examine the sensitivity of results on the horizontal domain size (A2DD) and horizontal resolution (A1HX). A2DD is identical to A2 except that the domain size is doubled (1024 km) and two cloud systems are initialized; that is, two gust front–type perturbations are introduced with their centers located 512 km apart. A1HX is identical to A1 except that the horizontal grid size is changed to 1 km (see Table 2). Since the differences among C0, A1, and A2 are very small, the results from

A2DD and A1HX will be compared with those of C0 only.

Figure 9 shows $\langle P \rangle$ for A2DD and A1HX. The time variation of $\langle P \rangle$ in both simulations is very similar to that of C0. The difference between A2DD and C0 is smaller than that between A1HX and C0. In A1HX, the time variation is smoother than in C0. Its difference from C0 is negligible in the first 7 h.

Figure 10 shows vertical profiles of fractional cloudiness, Q_{SW} and Q_{LW}, averaged over the entire domain and entire integration period. There is almost no significant difference in the fractional cloudiness at all levels except between 900 and 700 mb in A1HX. Here Q_{LW} shows some small differences in A2DD and A1HX. The overall impact due to the increase of the domain size or horizontal resolution is very small, however.

5. Summary

A broadband radiative transfer model (Harshvardhan et al. 1987) has been implemented into the UCLA cumulus ensemble model to explicitly simulate the cloud–radiation interactions and to examine the impacts of cloud–radiation interactions on the macroscopic behavior of cumulus ensembles. Several issues related to adequate calculation of radiative transfer processes in the CEM have been addressed. In the present implementation, the lowest CEM layer is divided into a thick layer and a very thin layer near the surface for the longwave radiation calculation. As in earlier studies (e.g., Wong et al. 1993), additional layers above the CEM top are added mainly for the accuracy of shortwave heating rates in the layers near the model top. The cloud optical properties in the radiation parameterization are formulated, based on Stephens et al. (1990). Diagnostic tests have been performed to compare the accuracy of this parameterization with results from a more complicated radiative transfer model (Wong et al. 1993).

Another important issue in the implementation is how to eliminate the spatial errors of the time-averaged radiative heating rates (over the time interval for calling a radiation module) due to infrequent computation of radiative transfer processes. Several sensitivity tests with fully interactive radiation have been performed to compare two methods for invoking the radiation module using three different time intervals, respectively. The time interval has to be very small for the conventional method, which keeps the heating rate constant until the radiation module is called again. The time interval can be at least twice as large with the accumulated method, which accumulates and averages cloud microphysical properties within the time interval as input to the radiation module and applies the amount of radiative heating over the time interval at the time when the radiation module is called. The time interval is mainly determined by the horizontal resolution of the model and the propagation speed of individual cloud cells; that is, a fast-moving cell in a high-resolution model requires a very small time interval. Additional sensitivity tests are also performed to justify the omission of the radiative effects of rapidly falling precipitating particles. A similar justification was obtained from the diagnostic tests.

Other sensitivity tests have been performed to examine to the adequacy of the domain size and horizontal resolution for studying the cloud–radiation interaction problems discussed in Part II (Xu and Randall 1995). A larger domain or a higher horizontal resolution does not significantly change the results.

The results presented here are from simulations of cumulus ensembles under idealized large-scale conditions, with a simple radiative transfer model. Some aspects of the conclusions need to be tested further with more complicated radiative transfer models under a variety of large-scale conditions.

Acknowledgments. Discussions with Professors Graeme Stephens and Harshvardhan, and Dr. Takmeng Wong are appreciated. The authors thank Prof. Dean Churchill and two anonymous reviewers for their valuable comments. This study was supported by the U.S. Department of Energy's Atmospheric Radiation Measurement program under Grant DE-FG02-92ER61363.

REFERENCES

Arakawa, A., 1975: Modeling clouds and cloud processes for use in climate models. *The Physical Basis of Climate and Climate Modelling, GARP Publ. Ser.*, No. 16, 181–197.

Businger, J. A., 1973: Turbulent transfer in the atmospheric surface layer. *Workshop on Micrometeorology,* D. E. Haugen, Ed., Amer. Meteor. Soc., 67–98.

Cess, R. D., and Coauthors, 1990: Intercomparison and interpretation of climate feedback processes in 19 atmospheric general circulation models. *J. Geophys. Res.*, **95,** 16 601–16 615.

Chen, S., and W. R. Cotton, 1988: The sensitivity of a simulated extratropical mesoscale convective system to longwave radiation and ice-phase microphysics. *J. Atmos. Sci.*, **45,** 3897–3910.

Chou, M.-D., 1984: Broadband water vapor transmission functions for atmospheric IR flux computations. *J. Atmos. Sci.*, **41,** 1775–1778.

——, and L. Peng, 1983: A parameterization of the absorption in the 15 μm spectral region with application to climate sensitivity studies. *J. Atmos. Sci.*, **40,** 2183–2192.

Churchill, D. D., and R. A. Houze Jr., 1991: Effects of radiation and turbulence on the diabatic heating and water budget of the stratiform region of a tropical cloud cluster. *J. Atmos. Sci.*, **48,** 903–922.

Dudhia, J., 1989: Numerical study of convection observed during the winter monsoon experiment using a mesoscale two-dimensional model. *J. Atmos. Sci.*, **46,** 3077–3107.

Fu, Q., and K. N. Liou, 1993: Parameterization of the radiative properties of cirrus clouds. *J. Atmos. Sci.*, **50,** 2008–2025.

——, S. K. Krueger, and K. N. Liou, 1995: Interactions between radiation and convection in simulated tropical cloud clusters. *J. Atmos. Sci.*, in press.

Gray, W. M., and R. W. Jacobson Jr., 1977: Diurnal variation of deep cumulus convection. *Mon. Wea. Rev.*, **105,** 1171–1188.

Harshvardhan, R. Davies, D. A. Randall, and T. G. Corsetti, 1987: A fast radiation parameterization for general circulation models. *J. Geophys. Res.*, **92,** 1009–1016.

——, D. A. Randall, T. G. Corsetti, and D. A. Dazlich, 1989: Earth radiation budget and cloudiness simulations with a general circulation model. *J. Atmos. Sci.*, **46,** 1922–1942.

Held, I. M., R. S. Hemler, and V. Ramaswamy, 1993: Radiative–convective equilibrium with explicit two-dimensional moist convection. *J. Atmos. Sci.*, **50,** 3907–3927.

Houze, R. A., Jr., 1977: Structure and dynamics of a tropical squall-line system. *Mon. Wea. Rev.*, **105,** 1540–1567.

Joseph, J. H., W. J. Wiscombe, and J. A. Weinman, 1976: The delta-Eddington approximation for radiative flux transfer. *J. Atmos. Sci.*, **33,** 2452–2459.

Krueger, S. K., 1988: Numerical simulation of tropical cumulus clouds and their interaction with the subcloud layer. *J. Atmos. Sci.*, **45,** 2221–2250.

——, Q. Fu, K. N. Liou, and H.-N. Chin, 1995: Improvements of an ice-phase micro-physics parameterization for use in numerical simulations of tropical convection. *J. Appl. Meteor.*, **34,** 281–287.

Lacis, A. A., and J. E. Hansen, 1974: A parameterization for the absorption of solar radiation in the earth's atmosphere. *J. Atmos. Sci.*, **31,** 118–133.

LeMone, M. A., and E. J. Zipser, 1980: Cumulonimbus vertical velocity events in GATE. Part I: Diameter, intensity, and mass flux. *J. Atmos. Sci.*, **37,** 2444–2457.

Lilly, D. K., 1988: Cirrus outflow dynamics. *J. Atmos. Sci.*, **45,** 1594–1605.

Lin, Y.-L., R. D. Farley, and H. D. Orville, 1983: Bulk parameterization of the snow field in a cloud model. *J. Climate Appl. Meteor.*, **22,** 1065–1092.

Lord, S. J., H. E. Willoughby, and J. M. Piotrowicz, 1984: Role of a parameterized ice-phase microphysics in an axisymmetric, nonhydrologic tropical cyclone model. *J. Atmos. Sci.*, **41,** 2836–2848.

Marshall, J. S., and W. Mck. Palmer, 1948: The distribution of raindrops with size. *J. Meteor.*, **5,** 165–166.

Miller, R. A., and W. M. Frank, 1993: Radiative forcing of simulated tropical cloud clusters. *Mon. Wea. Rev.*, **121,** 482–498.

Roberts, R. E., J. E. A. Selby, and L. M. Biberman, 1976: Infrared continuum absorption by atmospheric water vapor in the 8–12 μm window. *Appl. Opt.*, **15,** 2085–2090.

Rogers, C. D., 1968: Some extensions and application of the new random model for molecular band transmission. *Quart. J. Roy. Meteor. Soc.*, **94,** 99–102.

Stackhouse, P. W., Jr., and G. L. Stephens, 1991: A theoretical and observational study of the radiative properties of cirrus: Results from FIRE 1986. *J. Atmos. Sci.*, **48,** 2044–2059.

Stephens, G. L., S.-C. Tsay, P. W. Stackhouse Jr., and P. J. Flatau, 1990: The relevance of the microphysical and radiative properties of cirrus clouds to climate and climate feedback. *J. Atmos. Sci.*, **47,** 1742–1753.

Sui, C.-H., K.-M. Lau, W.-K. Tao, and J. Simpson, 1994: The tropical water and energy cycles in a cumulus ensemble model. Part I: Equilibrium climate. *J. Atmos. Sci.*, **51,** 711–728.

Tao, W.-K., J. Simpson, and S.-T. Soong, 1991: Numerical simulation of a subtropical squall line over the Taiwan Strait. *Mon. Wea. Rev.*, **119,** 2699–2723.

——, ——, C.-H. Sui, B. Ferrier, S. Lang, J. Scala, M.-D. Chou, and K. Pickering, 1993: Heating, moisture and water budgets of tropical and midlatitude squall lines: Comparisons and sensitivity to longwave radiation. *J. Atmos. Sci.*, **50,** 673–690.

van de Hulst, H., 1957: *Light Scattering by Small Particles.* Dover, 470 pp.

Webster, P. J., and G. L. Stephens, 1980: Tropical upper troposphere extended clouds: Inferences from Winter MONEX. *J. Atmos. Sci.*, **37,** 1521–1541.

Wong, T., G. L. Stephens, P. W. Stackhouse Jr., and F. P. J. Valero, 1993: The radiative budgets of a tropical mesoscale convective system during EMEX-STEP-AMEX experiment. II: Model results. *J. Geophys. Res.*, **98,** 8695–8711.

Xu, K.-M., 1993: Cumulus ensemble simulation. *The Representation of Cumulus Convection in Numerical Models of the Atmosphere,* K. A. Emanuel and D. J. Raymond, Eds., *Meteor. Monogr.*, No. 46, Amer. Meteor. Soc., 221–235.

——, and S. K. Krueger, 1991: Evaluation of cloudiness parameterization using a cumulus ensemble model. *Mon. Wea. Rev.*, **119,** 342–367.

——, and D. A. Randall, 1995: Impact of interactive radiative transfer on the macroscopic behavior of cumulus ensembles. Part II: Mechanisms for cloud–radiation interactions. *J. Atmos. Sci.*, **52,** 800–817.

——, A. Arakawa, and S. K. Krueger, 1992: The macroscopic behavior of cumulus ensembles simulated by a cumulus ensemble model. *J. Atmos. Sci.*, **49,** 2404–2420.

Zipser, E. J., 1977: Mesoscale and convective-scale downdrafts as distinct components of squall-line structure. *Mon. Wea. Rev.*, **105,** 1568–1589.